SUPER-ULTIMATE HEAT TRANSFER IN TURBULENT THERMAL CONVECTION BETWEEN HORIZONTAL POROUS WALLS

Fanyu Meng
Graduate School of Engineering Science
Osaka University
meng@tes.me.es.osaka-u.ac.jp

Shingo Motoki
Graduate School of Engineering Science
Osaka University
motoki.shingo.es@osaka-u.ac.jp

Genta Kawahara
Graduate School of Engineering Science
Osaka University
genta.kawahara.es@osaka-u.ac.jp

ABSTRACT

By implementing the immersed boundary method, numerical investigation into heat transfer and flow structure has been conducted in turbulent thermal convection between horizontal porous walls heated from below and cooled from above. We perform direct numerical simulation with high-order compact schemes for turbulent convection at the Rayleigh number $Ra = 10^6$–3×10^8. It is found that at low Ra, the Nusselt number Nu in the bulk region scales with $Ra^{1/3}$ as in the classical state, whereas at high Ra, Nu scales with $Ra^{1/2}$, implying the ultimate state in which the vertical heat flux is independent of thermal conductivity, i.e., the so-called anomalous thermal conduction. At low Ra, vertical (wall-normal) fluid motion is not excited in the near-wall region despite wall porosity, so that the classical state can be observed. At high Ra, large-scale thermal plumes appear even near the walls to significantly intensify the wall heat flux, leading to the ultimate state. In between these two distinct scaling ranges of Ra, more interestingly, we find super-ultimate behaviour $Nu \sim Ra$. This super-ultimate scaling is considered to be a consequence of full excitation of large-scale thermal plumes comparable with those in the ultimate state at high Ra and of less energy dissipation in the flow through porous media than in the ultimate state at high Ra. Extension of the super-ultimate behaviour to a higher-Ra range is also discussed.

Introduction

The canonical thermal flow system known as Rayleigh-Bénard convection is brought about by buoyancy in a horizontal fluid layer that is heated from below and cooled from above. The Rayleigh number and the Prandtl number, respectively defined as $Ra = g\alpha\Delta T H^3/(\nu\kappa)$ and $Pr = \nu/\kappa$, are important dimensionless parameters in this flow system, where g, α, κ, and ν stand for the acceleration of gravity, volumetric expansion coefficient, thermal diffusivity, and kinematic viscosity, respectively. The intensity of a heat flux is measured in relation to thermal conduction using the Nusselt number Nu. Long discussed has been the power law $Nu \sim Ra^\gamma$, where different values of the exponent γ show different states in this system. The classical scaling $Nu \sim Ra^{1/3}$ widely observed in experiments and numerical simulations was derived by Malkus

(1954) and Priestley (1954) using instability and dimensional analyses. Kraichnan (1962), on the other hand, forecasted an asymptotic final regime as $Nu \sim Pr^{1/2}Ra^{1/2}$ with a logarithm correction resulting from turbulent boundary layers. The most important implication is that in the ultimate state, heat transport cannot be dependent on kinematic viscosity or thermal diffusivity. By using numerical and experimental methods, several attempts have been made to reach the ultimate scaling; however, the effects of the wall even with surface roughness have been known to hinder heat transport from demonstrating the ultimate scaling (see e.g. Zhu *et al.*, 2019).

Kawano *et al.* (2021) has recently accomplished the ultimate scaling at large Rayleigh numbers in turbulent thermal convection between Darcy-type permeable walls on which the vertical velocity is given by the pressure fluctuation p as $w = \pm\beta p/\rho$ with a positive constant β (Jiménez *et al.*, 2001). Motivated by Kawano *et al.* (2021)'s introduction of permeable walls, we have investigated turbulent thermal convection between porous walls, and in this more realistic configuration, we have also achieved the ultimate heat transfer (Meng *et al.*, 2022). In this study, we report that the super-ultimate heat transfer $Nu \sim Ra$ can be attained in the intermediate range of Ra between the classical and ultimate regimes. We discuss the mechanism governing this super-ultimate transition in light of the observed phenomena and their relevance to the idealised configuration of Darcy-type permeable walls, which may provide us with additional insight into the extension of the super-ultimate heat transfer to a higher-Ra range.

Governing equations and flow configuration

Our governing equations are the Boussinesq equations which are the incompressible Navier–Stokes equations with the Oberbeck-Boussinesq approximation and the energy equation. To assure quasi-spectral precision, a staggered finite-difference algorithm Incompact3D developed by Laizet & Lamballais (2009) and Laizet & Li (2011) based on high-order compact schemes has been utilized. The detailed effects generated by the geometric structures in this flow system are created using the immersed boundary method. We use the free-fall velocity $U_f = (g\alpha\Delta T H)^{1/2}$ (ΔT and H being a temperature difference and a distance between the porous walls, respectively)

as a reference velocity. In this study, the Rayleigh number is changed in the range $Ra = 10^6$–3×10^8 for $Pr = 1$.

The Boussinesq equations, which employs the Oberbeck-Boussinesq approximation in the Navier-Stokes equation are our governing equations,

$$\frac{\partial \boldsymbol{u}}{\partial t} + (\boldsymbol{u} \cdot \nabla)\boldsymbol{u} = -\frac{1}{\rho}\nabla p + \nu \nabla^2 \boldsymbol{u} + g\alpha T \boldsymbol{e}_z + \boldsymbol{f}_b \quad (1)$$

$$\nabla \cdot \boldsymbol{u} = 0 \quad (2)$$

$$\frac{\partial T}{\partial t} + (\boldsymbol{u} \cdot \nabla)T = \kappa \nabla^2 T + q_b \quad (3)$$

in which, $\boldsymbol{u}(\boldsymbol{x},t) = u\boldsymbol{e}_x + v\boldsymbol{e}_y + w\boldsymbol{e}_z$ and $T(\boldsymbol{x},t)$ denote the velocity field and temperature field respectively. The velocity field and temperature field in this case follow the periodic boundary conditions in the horizontal x- and y-directions with the same length as $L_x = L_y = H$. The $\boldsymbol{f}_b$ and q_b denote the force field and heat source term on account of the implemented immersed boundary method, respectively. We use the buoyancy-induced terminal velocity, $U_f = (g\alpha\Delta TH)^{1/2}$ as a reference velocity scale. Pr and Ra are control parameters in the system and the Pr is set to unity in this study. Moreover, the aspect ratio i.e., the ratio of the horizontal extent to the height is also a control parameter. The boundary conditions for computational domain of liquid parts have been set as blow,

$$u(z=0) = u(z=3H) = w(z=0) = w(z=3H) = 0 \quad (4)$$

$$T(z=0) = T(z=3H) = 0 \quad (5)$$

and the boundary conditions for the solid parts are imposed as no-slip and isothermal,

$$u = v = w = 0 \quad (6)$$

$$T(z < H|_{\text{solid}}) = \Delta T \quad (7)$$

$$T(z > 2H|_{\text{solid}}) = 0 \quad (8)$$

The intensity of the convection will be quantified in terms of the heat flux resulting from the temperature difference between the top and bottom walls given by Nusselt number Nu,

$$Nu = \frac{-\kappa \frac{\mathrm{d}\langle T\rangle_{xyt}}{\mathrm{d}z} + \langle wT\rangle_{xyt}}{\kappa \Delta T / H} \quad (9)$$

where $< \cdot >_{xyt}$ denotes the horizontal and time average on the variables at the center of domain.
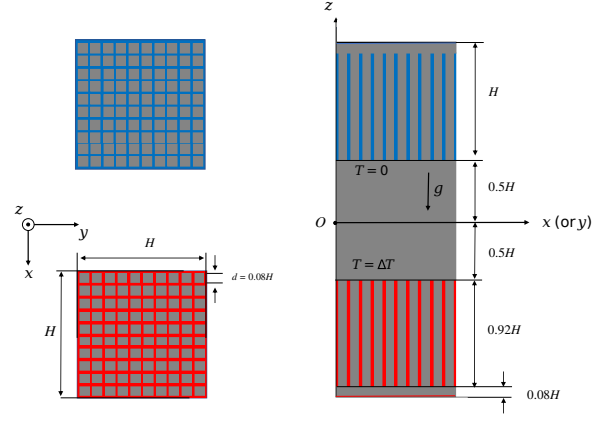

Figure 1: The geometry of porous walls and flow configuration. The lower, hotter (or upper, cooler) porous media and bottom (or top) wall are coloured red (or blue). The fluid is coloured grey.

The geometry and flow configuration are shown in Figure 1. The velocity and the temperature are supposed to be periodic in the horizontal x- and y-directions with the same periodicity $L_x = L_y = H$. The lower, hotter (or upper, cooler) porous wall with temperature $T = \Delta T$ (or $T = 0$) possesses a 10×10 matrix of vertical square holes in the periodic box. The hole width is $0.08H$. There is a plenum chamber with a height $0.08H$ between the lower (or upper) porous wall and the bottom (or top) wall with the consistent temperature $T = \Delta T$ (or $T = 0$).

Scaling property and energy dissipation

It is seen from Figure 2 that by introducing porosity in the walls, the ultimate scaling $Nu \sim Ra^{1/2}$ can be achieved at high Rayleigh number $Ra \gtrsim 10^8$. At low Rayleigh number around $Ra = 10^6$, on the other hand, Nu is nearly consistent with that in the conventional non-porous case and exhibits the classical scaling $Nu \sim Ra^{1/3}$, indicating that the wall porosity has no significant effect on heat transfer.

The most remarkable observation in Figure 2 is that super-ultimate transient $Nu \sim Ra$ appears in between the classical and the ultimate regimes, significantly exceeding the ultimate scaling $Nu \sim Ra^{1/2}$.

We have confirmed that at higher $Ra \gtrsim 10^7$ large-scale thermal plumes are induced by the wall porosity and highly intensify thermal convection and hence heat transfer (figure not shown). The induced large-scale thermal structures fully extend from one porous wall to the other, so that they are characterised in terms of the length scale H and the temperature scale ΔT. Those large-scale strong thermal plumes are the key to the achievement of the (super-) ultimate state.

Figure 3 displays the average local dissipation inside the near-wall region, which is known to be the primary contributor to the overall energy dissipation in the system. From this image, it is evident that the dissipation diminishes as the Ra drops for lower values of Ra. The behaviour of normalized dissipation is typically laminar. For higher values of Ra, the dissipation shown in Figure 3 also increases as Ra grows. The shift in behaviour can be related to the formation of dissipative vortical structures surrounding the porous surface. At a Reynolds number of 10^8, the energy dissipation in the system is sufficient to prevent the velocity fluctuation from exceeding U_f, but it does scale with U_f, resulting in the ultimate scaling.
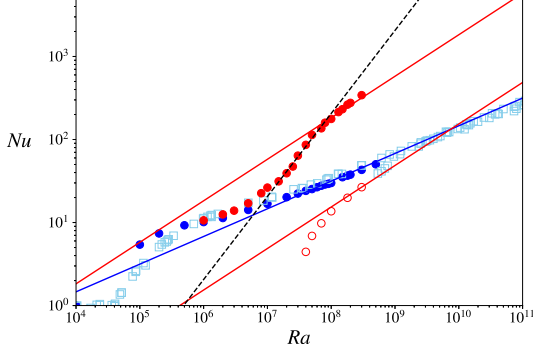
Figure 2: Nusselt number Nu as a function of Rayleigh number Ra. The blue and red lines represent the classical scaling $Nu \sim Ra^{1/3}$ and the ultimate scaling $Nu \sim Ra^{1/2}$, respectively. The black dashed line denotes the super-ultimate scaling $Nu \sim Ra$. The red filled and open circles represent Nu in the bulk region and the chamber region, respectively, in the porous wall case. The blue circles denote Nu in the non-porous wall case. The sky-blue squares are taken from the experimental data in a non-porous cylindrical cell (Chavanne et al., 2001).
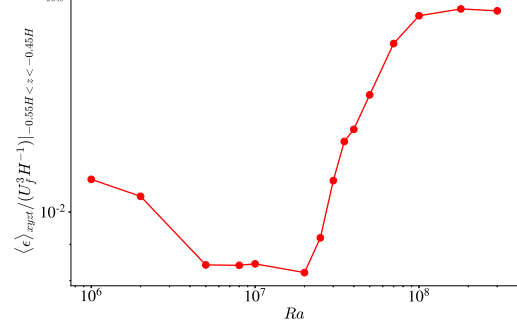

Figure 3: The value of local energy dissipation normalized with U_f^3/H as a function of the Rayleigh number in the near-wall region from $z = -0.55H$ to $z = -0.45H$.

Ra can be easily obtained as below,

$$ Nu \sim \frac{H}{\kappa \Delta T} Tw \sim \frac{H}{\kappa \Delta T} TU_f Ra^{1/2} \sim Ra^{1/2} Ra^{1/2} \sim Ra \quad (10) $$

in which, the $Nu \sim Ra$ scaling law in transition process is consistent with the results in Figure 2.

The presence and distribution of vortical structures can provide as evidence for the three stages of classical, transition, and ultimate, as they represent variations in the energy dissipation rate not only along the wall but also in the holes. As mentioned in the study by Meng et al. (2022), when the ultimate scaling limit is exceeded ($Nu \sim Ra$), specifically at Ra values of 1×10^7 and 7×10^7, it is observed that energy dissipation is distributed within the porous medium, while the vortical structure does not contribute significantly. This lack of vortical dissipation leads to an actual dissipation rate that exceeds Taylor's dissipation law, $\epsilon \sim U_f^3/H$. At a Rayleigh number of 1.8×10^8, the porous medium experiences the penetration of smoother vortical structures. This penetration is crucial for ensuring adequate energy dissipation within the system. Specifically, the overall energy dissipation rate of the system will be equivalent to Taylor's dissipation rate. As Ra increases to 3×10^8, the simultaneous occurrence of energy dissipation and vortical structures indicates that the stretching of the vortical structure becomes the primary mechanism for dissipating energy in the system. Furthermore, the vortical structures become dominant within the region where energy dissipation occurs in the porous holes. This occurrence is as well consistent with the result represented in Figure 3, indicating that the dissipation of the entire system has reached a saturated state, as the process of transitioning to the final state has been finished.

The transition process can also be interpreted with the help of the scaling relationships between the RMS of vertical velocity, energy dissipation rate normalized with U_f^3/H in the bulk region from $z = -0.5H$ to $z = 0.5H$. We have confirmed from the relationships these values that, as whole the system enters the transition process, $Ra \geq 2 \times 10^7$, the RMS of vertical velocity normalized by U_f can be scaled with $Ra^{1/2}$, $w/U_f \sim Ra^{1/2}$. Meanwhile, the energy dissipation rate normalized with U_f^3/H can also be scaled with $Ra^{1/2}$, $\epsilon/(U_f^3/H) \sim Ra^{1/2}$. The scaling relationship between Nu and

Discussion and outlook

Let us recall Kawano et al. (2021)'s argument on the ultimate state between idealised permeable walls on which $w = \pm \beta p/\rho$ are imposed. If we suppose that the flow through the wall holes is laminar, we have $\beta \sim d^2/(\nu \ell)$, d and ℓ being the hole size and the hole length, respectively. The dimensionless form of this estimate is $\beta U_f \sim (d/H)^2 (\ell/H)^{-1} Pr^{-1/2} Ra^{1/2}$. In the present configuration of fixed geometry for $Pr = 1$, the porous walls are more permeable as $\beta U_f \sim Ra^{1/2}$ with increasing Ra. The energy budget in the idealised permeable wall case is given by

$$ g\alpha \langle wT \rangle_{xyzt} = \epsilon + \frac{2}{\beta H} \left\langle w^2 \right\rangle_{xyt}\bigg|_w - \frac{1}{H} \left\langle w^3 \right\rangle_{xyt}\bigg|_w \quad (11) $$

where ϵ is energy dissipation. The left-hand side represents buoyancy power, while the second and the third terms on the right-hand side denote pressure power on the permeable walls and outflow kinetic energy (which has been found to be insignificant) across the permeable walls, respectively. In the ultimate state, the pressure power on the permeable walls has been found to be comparable with the buoyancy power and the energy dissipation. Taking the velocity scale of the large-scale thermal structures as W, we have

$$ \frac{W^2}{\beta H} \sim g\alpha W\Delta T \sim \epsilon \quad (12) $$

implying that

$$ W \sim \beta U_f^2 \quad (13) $$

In the present configuration for fixed geometry represented by $\beta U_f \sim Ra^{1/2}$ as discussed above, therefore, we obtain the velocity scale and the energy dissipation in the super-ultimate
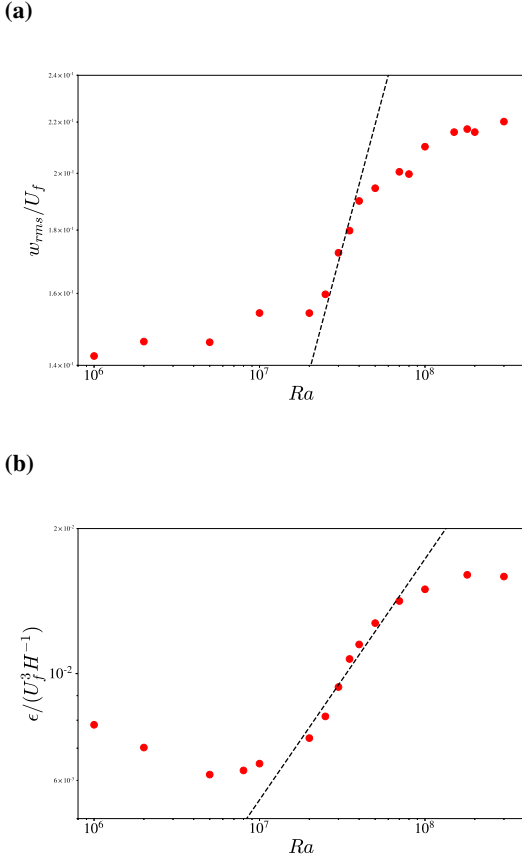
3

(a)

(b)

Figure 4: (a) Root-mean-square (rms) vertical velocity w_{rms} in the bulk region normalised by U_f. (b) Energy dissipation rate ϵ in the bulk region normalised by U_f^3/H. The black dashed lines denote the super-ultimate scaling (a) $w_{rms}/U_f \sim Ra^{1/2}$ and (b) $\epsilon/(U_f^3/H) \sim Ra^{1/2}$.

state as

$$W \sim Ra^{1/2} U_f \qquad (14)$$

$$\epsilon \sim Ra^{1/2} \frac{U_f^3}{H}. \qquad (15)$$

Now, the turbulent heat flux in the super-ultimate state is estimated as $W\Delta T \sim Ra^{1/2} U_f \Delta T$, suggesting that the corresponding Nusselt number is given by $Nu \sim W\Delta T/(\kappa\Delta T/H) \sim$

$Ra^{1/2}(U_f\Delta T/\kappa\Delta T/H) \sim Pr^{1/2} Ra$. This argument can interpret the super-ultimate transient $Nu \sim Ra$ in Figure 2 as well as $w_{rms}/U_f \sim Ra^{1/2}$ and $\epsilon/(U_f^3/H) \sim Ra^{1/2}$ in Figure 4.

At high $Ra \gtrsim 10^8$, flow separation and resulting dissipative vortices lead to a significant local pressure drop in the entrance (or exit) of the holes. Consequently, we have seen the saturation down to the ultimate state $Nu \sim Ra^{1/2}$ in Figure 2. However, the above argument suggests that if we implement longer (or smaller) holes in the walls so that the local pressure drop may be much smaller than a friction pressure drop, then the super-ultimate behaviour can be extended to a higher-Ra range.

REFERENCES

Chavanne, X., Chilla, F., Chabaud, B., Castaing, B. & Hebral, B. 2001 Turbulent rayleigh–bénard convection in gaseous and liquid He. *Physics of Fluids* **13**, 1300–1320.

Jiménez, J., Uhlmann, M., Pinelli, A. & Kawahara, G. 2001 Turbulent shear flow over active and passive porous surfaces. *Journal of Fluid Mechanics* **442**, 89–117.

Kawano, K., Motoki, S., Shimizu, M. & Kawahara, G. 2021 Ultimate heat transfer in 'wall-bounded' convective turbulence. *Journal of Fluid Mechanics* **914**, A13.

Kraichnan, R. H. 1962 Turbulent thermal convection at arbitrary Prandtl number. *The Physics of Fluids* **5** (11), 1374–1389.

Laizet, S. & Lamballais, E. 2009 High-order compact schemes for incompressible flows: A simple and efficient method with quasi-spectral accuracy. *Journal of Computational Physics* **228**, 5989–6015.

Laizet, S. & Li, N. 2011 Incompact3d: A powerful tool to tackle turbulence problems with up to O (10^5) computational cores. *International Journal for Numerical Methods in Fluids* **67**, 1735–1757.

Malkus, W. V. 1954 The heat transport and spectrum of thermal turbulence. *Proceedings of the Royal Society of London. Series A. Mathematical and Physical Sciences* **225** (1161), 196–212.

Meng, F., Motoki, S. & Kawahara, G. 2022 Ultimate heat transfer in turbulent thermal convection between porous walls. In *Proceedings of 12th International Symposium on Turbulence and Shear Flow Phenomena (TSFP12)*.

Priestley, C. H. B. 1954 Convection from a large horizontal surface. *Australian Journal of Physics* **7** (1), 176–201.

Zhu, X., Stevens, R. J., Shishkina, O., Verzicco, R. & Lohse, D. 2019 Scaling enabled by multiscale wall roughness in Rayleigh–Bénard turbulence. *Journal of Fluid Mechanics* **869**, R4.